



ELSEVIER

Physica D 167 (2002) 183–196

PHYSICA D

www.elsevier.com/locate/physd

# Chaotic mixing and transport in wavy Taylor–Couette flow

Alp Akonur<sup>1</sup>, Richard M. Lueptow\*

*Department of Mechanical Engineering, Northwestern University, 2145 Sheridan Road, Evanston, IL 60208-3111, USA*

Received 30 July 2001; received in revised form 15 March 2002; accepted 5 April 2002

Communicated by R.P. Behringer

## Abstract

Chaotic transport and mixing in wavy cylindrical Couette flow has been studied in some detail, but previous studies have been limited to the velocity field at transition from Taylor–Couette flow to wavy flow or have used phenomenological, computational, or theoretical models of the flow. Recent particle image velocimetry measurements of wavy vortex flow provide the experimental three-dimensional, three-component velocity field at conditions well above the transition to wavy flow. Using this experimental velocity field, fluid tracer particles were tracked computationally to determine the nature of the mixing. The results show how mixing is enhanced with increasing rotating Reynolds number as a consequence of increased stretching and folding that occurs in meridional, latitudinal, and circumferential surfaces. The axial particle transport increases with the rotating Reynolds number as a consequence of stretching and folding within the vortices and the axial transport between vortices, both related to the waviness of the flow, as well as increased vortex strength. The calculated effective dispersion coefficient is very similar to that found experimentally and computationally confirming that chaotic advection is the mechanism responsible for enhanced mixing in wavy vortex flow.

© 2002 Elsevier Science B.V. All rights reserved.

*Keywords:* Chaotic advection; Taylor–Couette; Mixing; Effective diffusion

## 1. Introduction

Cylindrical Couette devices have often been proposed as mixing devices in applications such as catalytic chemical reactors, rotating filtration devices, and bioreactors [1–3]. These devices are based on an inner cylinder (IC) rotating within a fixed outer cylindrical shell. The idea in many of these devices is to optimally mix the fluid in the annulus while minimizing the local shear stresses throughout most of the annulus. In a cylindrical Couette device, Taylor vortex flow, consisting of counter-rotating, toroidal vortices stacked in

the annulus of the device, occurs due to a centrifugal instability above a particular critical Reynolds number,  $Re_c = r_i \Omega d / \nu$ , where  $r_i$  is the radius of the IC,  $\Omega$  the rotational speed,  $d$  the gap between the cylinders, and  $\nu$  the kinematic viscosity. This critical Reynolds number depends on the ratio of the radii of the inner to outer cylinders (OCs),  $\eta = r_i / r_o$ . Further increasing the Reynolds number to approximately  $1.2Re_c$  (for the radius ratios considered here) results in an azimuthal waviness in the vortices, known as wavy vortex flow.

Cylindrical Couette devices are often operated in the wavy vortex flow regime to enhance mixing. Computational models and particle image velocimetry (PIV) measurements of the velocity field in wavy cylindrical Couette flow have shown that, unlike non-wavy Taylor vortex flow, wavy vortices are not independent

\* Corresponding author. Tel.: +1-847-491-4265; fax: +1-847-491-3915.

E-mail address: r-lueptow@nwu.edu (R.M. Lueptow).

<sup>1</sup> Currently at Baxter Healthcare Corporation.

toroidal cells [4–6]. Instead, for wavy flow in a vertical cylindrical Couette flow device, regions of upward (downward) deformation of a vortex correspond to regions of upward (downward) axial flow. These regions of axial flow wind axially around the vortices from the inner to the outer cylinder and back. In any given meridional plane, over the period of one azimuthal wave, there is initially an upward flow winding around the vortices, followed by flow into alternate vortices from adjacent vortices, followed by downward flow winding around the vortices, completing the cycle with flow out of alternate vortices into adjacent vortices. Up to 50% of the volume of a vortex can be transported into and out of a vortex in one azimuthal wave period [5]. Furthermore, the regions of axial flow move back and forth in the azimuthal direction, depending on the phase of the wave [6]. In addition to the axial fluid transport, the vortices oscillate both axially, as is evident from flow visualization, and radially [5,6].

Axial mixing and dispersion in wavy vortex flow has been the recent focus of research from the standpoint of chaotic advection [7–13]. The axisymmetric cellular structure of non-wavy Taylor vortex flow results in a set of nested streamtubes (KAM tori) for each vortex with a dividing streamsurface (invariant surface) between adjacent vortices. Consequently, molecular diffusion is the only mechanism for transport within a vortex or between vortices. However, wavy vortex flow leads to two mechanisms that bring about the chaotic motion of fluid particles [12]. First, since the velocity field depends on all three spatial coordinates, streamtubes are destroyed leading to chaotic particle paths and intra-vortex mixing [9]. Secondly, the waviness breaks the streamsurface between neighboring vortices leading to substantial inter-vortex transport [5,9].

Several models of chaotic particle motion in wavy cylindrical Couette flow and the related Bénard convection flow have been explored. Broomhead and Ryrie [7] and Ryrie [8] devised a model of the cylindrical Couette velocity field just above the transition to traveling azimuthal waves by adding small temporally and spatially varying periodic disturbances to an axisymmetric model of non-wavy vortex flow. Based on this model, they were able to show that transport between vortices is possible even in the absence of

molecular diffusion and that particles passing from one vortex to another follow chaotic trajectories resulting in an enhanced effective diffusivity, or axial dispersion. Similarly, Solomon and Gollub [14,15] demonstrated enhancement of diffusivity in time-periodic Bénard convection both experimentally and via perturbations of a two-dimensional vortex model. Ashwin and King [9] used a very different approach in which they tracked fluid particles computationally in the velocity field from the perturbation solution for wavy Taylor vortex flow in a narrow gap just above the onset of waviness [16]. Their results indicated that some particles cross to adjacent vortices, although the cores of vortices remain isolated from one another.

The recent work of Rudman [10] and Rudolph et al. [11] most closely parallel the work we present here. Rudman analyzed the effective diffusion due to chaotic advection using particle tracking in a numerically modeled velocity field for wavy vortex flow considering rotating Reynolds numbers well above the transition to wavy vortex flow. He found that while fluid particles can be trapped in vortex cores under some conditions, under other conditions the entire flow appears to be chaotic. He also found that the Schmidt number based on an effective axial diffusivity related to chaotic advection decreases with increasing rotating Reynolds number, asymptoting to a value that indicates chaotic advection plays an important role in mixing. Rudolph et al. used a phenomenological stream function model of velocity field based on experimental measurements above the transition to wavy vortex flow in a meridional plane. While the model neglected the azimuthal component of velocity, it clearly showed the chaotic nature of the velocity field and the increased axial transport due to chaotic advection with increasing Reynolds number.

For completeness, we note that axial mixing and dispersion has also been studied from a more practical standpoint for the application of mixing in cylindrical Couette devices [1,2,17–23]. In many of these studies, the axial dispersion in cylindrical Couette flow was measured using dye concentration or tracer techniques.

In this paper we investigate the chaotic nature of the velocity field and the effective axial dispersion

based on experimental axial, azimuthal, and radial velocity components measured using PIV [5,6]. These measurements are unique in that they provide the time-resolved velocity field in three dimensions. Using this experimental velocity field, we track fluid particles computationally. This approach differs significantly from the approaches used by Broomhead and Ryrie [7], Ryrie [8], Ashwin and King [9], Rudman [10], or Rudolph et al. [11] in that the velocity field is experimentally measured, not a model of the velocity field. Thus, the degree of vortex distortion and transport between vortices is based on physical measurements rather than analytically convenient perturbations of non-wavy vortices or computational models. Furthermore, our approach permits us to consider flow conditions well above the transition from non-wavy Taylor–Couette flow to wavy vortex flow. This differs from the studies of Broomhead and Ryrie [7], Ryrie [8], or Ashwin and King [9], which are inherently limited to conditions very near the onset of the azimuthal waviness. Our objective here is to use the experimentally measured wavy vortex flow to investigate the relationship between the physics of the flow and the non-turbulent chaotic transport and mixing processes.

## 2. Experimental velocity field

A unique aspect of the work described in this paper is that the time-resolved, three-dimensional velocity field for wavy vortex flow was experimentally determined, unlike previous studies where the velocity field was computationally determined [10], theoretically based [9], or a phenomenological model [7,8]. The velocity field was measured using PIV. Pairs of digital images of illuminated seed particles in a laser-illuminated plane were obtained at a slight time delay using a CCD camera. The spatial cross-correlation between corresponding small regions in the two images provides the average displacement of particles in that region from which the statistically averaged velocity of the seed particles, and hence the fluid, in the illuminated plane can be determined. Calculating the velocity at a grid of locations in the illuminated plane provides the in-plane velocity field for the entire image. Sequen-

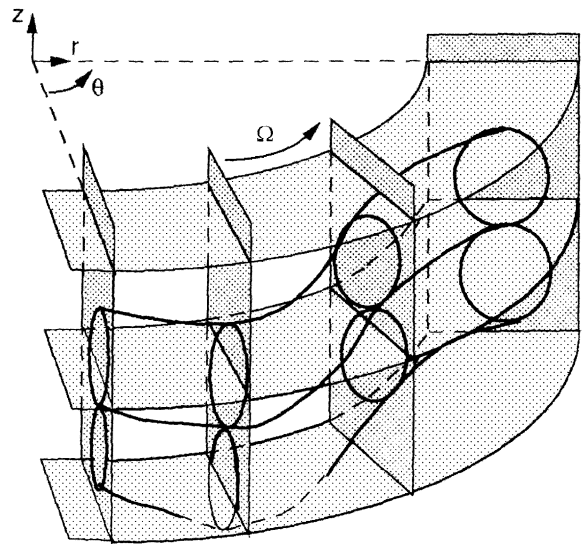


Fig. 1. Sketch of PIV measurement planes. Measurements in meridional ( $r$ - $z$ ) planes were matched to measurements in latitudinal ( $r$ - $\theta$ ) planes by shifting the planes to minimize the difference in the radial velocity, which was measured in both cases.

tially obtained image pairs provide the time-resolved velocity field in the plane for an unsteady flow.

The velocity field used in this study was obtained from PIV measurements of the velocity field in meridional ( $r$ - $z$ ) and latitudinal ( $r$ - $\theta$ ) planes as shown in Fig. 1 [5,6]. Since the velocity field in wavy vortex flow consists of wavy vortices with the waviness traveling azimuthally at about one-third of the velocity of the IC, measurements in a single meridional plane as the wave passes through the plane provide the radial ( $v_r$ ) and axial ( $v_z$ ) velocities as a function of time, or, equivalently, as a function of the phase of the traveling wave [5]. Likewise, PIV measurements in a series of latitudinal planes perpendicular to the axis of rotation and slicing through a vortex pair at uniform axial positions provides the radial ( $v_r$ ) and azimuthal ( $v_\theta$ ) velocities [6]. By matching the radial velocities in eight meridional planes (corresponding to one azimuthal wave) and 12 latitudinal planes (corresponding to the axial extent of two vortices), the entire time-resolved, three-dimensional, three-component velocity field can be obtained [6].

The velocity field for wavy vortex flow has been measured for a radius ratio of  $\eta = r_i/r_o = 0.82$ , where

$r_i$  is the radius of the IC and  $r_o$  the radius of the OC. At this radius ratio, the transition from nonvortical flow to non-wavy vortical flow (Taylor vortex flow) occurs at a critical Reynolds number of  $Re_c = r_i \Omega d / \nu = 100$  [24]. Wavy vortices were first readily detectable at a reduced Reynolds number of  $\varepsilon = Re / Re_c - 1 = 0.28$ . Measurements were made for  $\varepsilon = 0.28, 1.48,$  and  $5.03$ . The velocities measured using PIV were smoothed to minimize experimental noise and interpolated onto a grid with the resolution  $\Delta r, \Delta \theta,$  and  $\Delta z$  noted in Table 1. Also indicated in the table are the number of azimuthal waves,  $m$ , the axial wavelength for a vortex pair,  $\lambda,$  and the period for a travelling azimuthal wave,  $T$ .

The experimental velocity field is shown in Fig. 2. This figure shows the radial and axial velocity vectors in meridional plane overlaid with azimuthal velocity contours for approximately the same phase in the azimuthal wave for the three reduced Reynolds numbers. The lower boundary in each frame is the rotating IC, and the upper boundary is the fixed OC. The magnitude of the velocity vectors is indicated by the vector below the lowest frame.

Some characteristics of wavy vortex flow are evident in the figure. The vortical motion, clearly evident in the velocity vectors, increases in intensity with increasing Reynolds numbers. The vortical motion causes the deformation of the azimuthal contours as high azimuthal momentum fluid is carried outward at outflow boundaries and low azimuthal momentum fluid is carried inward at inflow boundaries. In addition, there is significant leftward axial transport between vortices as fluid winds around the vortices [5]. This axial fluid transport depends on the phase of the azimuthal wave. One half wave period later, the axial transport is rightward. In fact, there are streams of rightward and leftward axial flow in the annulus

Table 1  
Number of waves, wavelength, and resolution of interpolated velocity field

$\varepsilon$	$m$	$\lambda/d$	$\Delta r/d$	$\Delta \theta$ (°)	$\Delta z/d$	$T r_i \Omega / d$	$T$ (s)
0.28	2	2.16	0.050	1	0.090	33	7.96
1.48	4	2.16	0.050	1	0.090	21	2.63
5.03	4	2.18	0.050	1	0.068	25	1.18

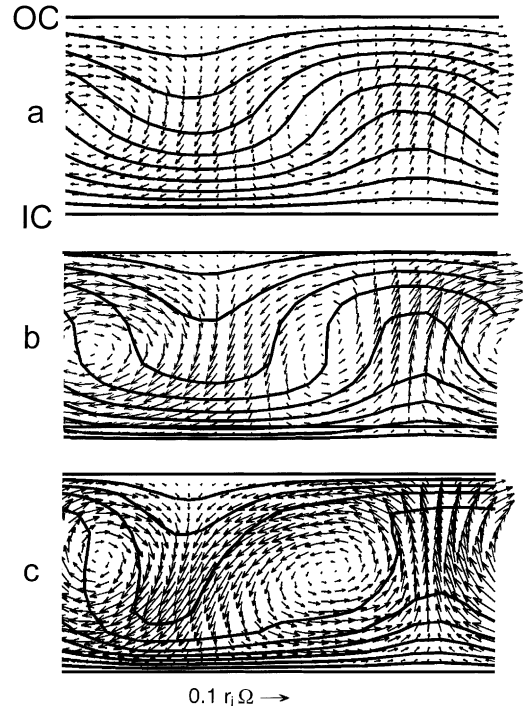


Fig. 2. Radial ( $v_r$ ) and axial ( $v_z$ ) velocity vectors in a meridional plane overlaid with azimuthal velocity contours shown at the same approximate phase of the azimuthal wave: (a)  $\varepsilon = 0.28$ , (b)  $1.48$ , (c)  $5.03$ . The azimuthal velocity contours are equally spaced between  $0$  at the OC and  $1.0 r_i \Omega$  at the IC.

that wind from the inner to outer cylinder and back as well as winding azimuthally about one-half azimuthal wavelength [6]. At  $\varepsilon = 1.48$  as much as 54% of the fluid in a vortex is transferred in and out of the vortex over one wave period due to the axial transport of fluid. At  $\varepsilon = 0.28$  and  $5.03$  the amount of axial fluid transport is somewhat less, but still substantial, 40 and 45%, respectively [5]. Although it is not shown in the figure, the vortex centers oscillate both axially and radially due to the waviness of the vortices [5]. In addition, the azimuthal velocity at the vortex centers is about that of the traveling azimuthal wave evident upon flow visualization of the system [6].

### 3. Passive fluid particle tracking

From kinematical standpoint, mixing is the stretching and folding of material surfaces. To investigate

mixing and transport in the flow field we track passive “fluid particles” having a density identical to the fluid and an infinitesimally small size. This is equivalent to calculating fluid pathlines according to the equations

$$\frac{dr}{dt} = v_r, \quad \frac{dz}{dt} = v_z, \quad \frac{d\theta}{dt} = \frac{v_\theta}{r} \quad (1)$$

using a fourth order Runge–Kutta scheme to find the new position based on the original position and the velocity at that position. The velocity was interpolated based on the discrete three-dimensional experimental velocity field, which extended axially two vortices (one axial wavelength) and was repeated periodically. In order to validate the particle tracking code, particles were tracked in a mathematically generated velocity field that was mapped on to a three-dimensional polar grid with spacing similar to the experimental velocity field. The mathematically generated velocity field consisted of a circular velocity in a meridional plane (like a Taylor vortex) together with a constant azimuthal velocity. Although the velocity field was nonphysical (it does not satisfy continuity), it has similarities to vortical flow in a cylindrical Couette device. Furthermore, it allowed testing the accuracy of the integration and interpolation schemes by comparing the numerically calculated particle positions after a long time with the exact solution. This test showed that the integration and interpolation schemes were quite robust, at least for this nonphysical velocity field. Because of the very short time step used in the calculations, the typical error in the radial position of a tracked particle was less than 0.1% after 370 revolutions around the circular path.

In this paper, we show the particle paths or positions as a function of nondimensional time,  $t/T$ , where  $T$  is the period of one azimuthal wave passing through a fixed meridional plane. Values for  $T$  are indicated in Table 1, both dimensionally and nondimensionally. The time step used in particle tracking calculations was  $0.002T$ . The total time for which the particles can be tracked is somewhat limited. In complex flow fields, seemingly inconsequential computational errors related to discretization, time-integration, and round-off can substantially alter the particle tracking results, even for an exact solution to the flow field. These errors

increase exponentially with tracking time for chaotic flows [25]. When the flow field is experimentally determined, the inherent experimental error has the same effect as the computational errors. However, the experimental errors can be much larger. The error in the experimental velocity field is estimated to be about 1–4% of the velocity of the IC. Since the axial and radial velocities are substantially less than the velocity of the IC, the error in the radial or axial velocities can build up quickly. Thus, it is quite difficult to track particles for long times using the experimental velocity field. Fortunately, results useful in understanding the chaotic nature of the velocity field are obtained from tracking particles over relatively short times. In fact, tracking particles over relatively short times is advantageous in producing more easily interpreted particle trajectories, which is the focus of this paper.

#### 4. Particle tracking results

We first examine fluid mixing from a kinematical standpoint as the stretching and folding of material lines by marking particular particles in a region of the flow. Because the azimuthal velocity varies substantially from the inner to the outer cylinder, we consider the deformation of an axial line of fluid particles that begins at different radial positions to see how the deformation varies. Fig. 3 shows the deformation of a line of 2000 particles initially at  $(r - r_i)/d = 0.25, 0.50, 0.75$  for each of the three reduced Reynolds numbers considered. The number of particles tracked was large enough to produce smooth curves with sufficient resolution to show details, while keeping the computation times reasonable. The line of particles initially extends a distance of  $2\lambda$ , approximately from the center of one clockwise (CW) vortex to another. The line of particles is “released” from an initial azimuthal position corresponding to the meridional plane in which the azimuthal wave is at its rightmost axial position to permit comparison between equivalent initial positions at different Reynolds numbers. For each Reynolds number in Fig. 3, the upper horizontal solid line is the OC and the lower solid line is the IC. The curves show the line of particles at  $t = 0, 0.5T$ , and  $1.0T$ .

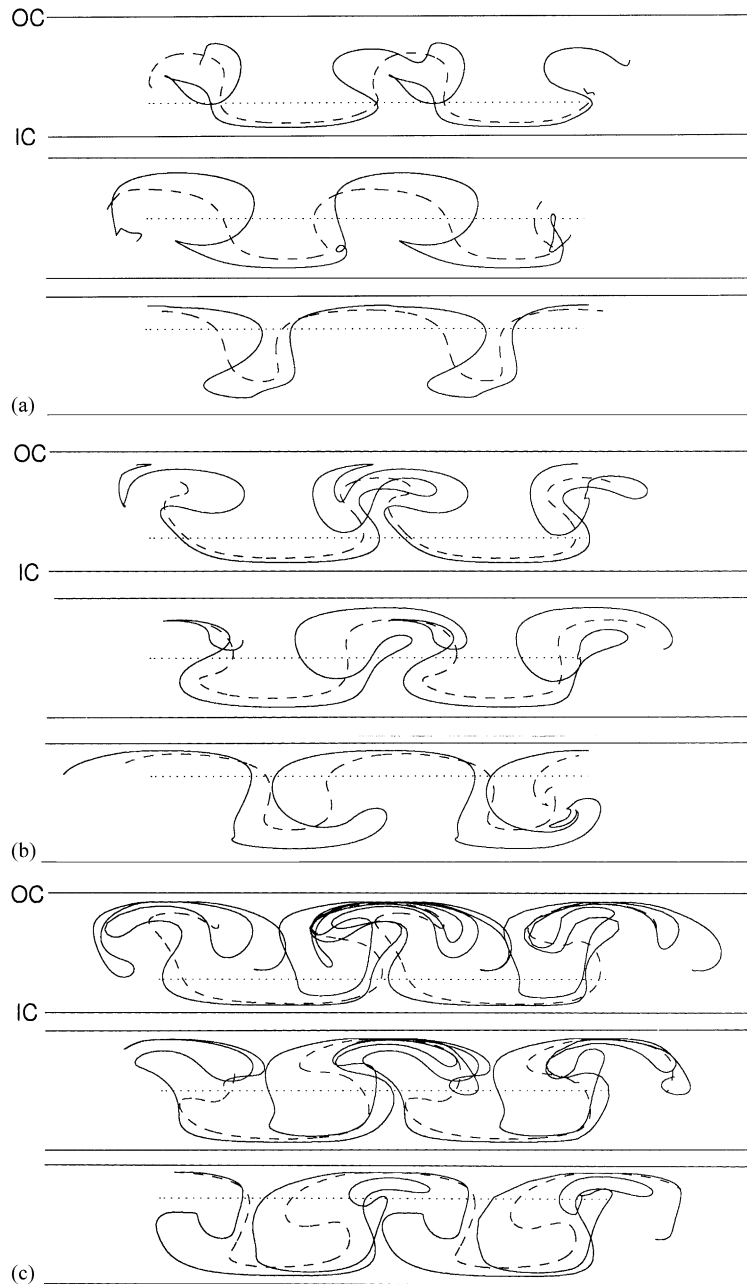


Fig. 3. Deformation of an axial line of 2000 particles initially about  $2\lambda$  long at  $(r - r_1)/d = 0.25$  (top), 0.5 (middle), 0.75 (bottom) for  $t = 0$  (dotted),  $0.5T$  (dashed), and  $1.0T$  (solid) viewed in a meridional plane: (a)  $\varepsilon = 0.28$ , (b) 1.48, (c) 5.03.

For all initial radial positions shown in Fig. 3, the line of particles is subject to extensive folding and stretching resulting in horse-shoe shaped structures characteristic of mixing in a chaotic flow [26,27].

Further, note the self-similar structure exhibited by folded elements as time evolves. For example in the upper frame of Fig. 3(b), a relatively thin tongue is enclosed by a similar larger tongue at  $1.0T$ . The degree

of folding and stretching increases with the Reynolds number,  $\varepsilon$ , which is somewhat surprising given that the total axial fluid transport between vortices is greater for  $\varepsilon = 1.48$  than for either of the other two Reynolds numbers [5]. But from Fig. 2, it is evident that the vortices increase in strength with Reynolds number. Thus, it appears that the increasing strength of the vortical structures with  $\varepsilon$  enhances chaotic advection even though the axial transport between vortices decreases somewhat at the highest Reynolds number. However, it is quite clear that flux between vortices is necessary for significant axial dispersion. Thus, the vortex strength apparently acts together with axial transport between vortices to enhance the stretching and folding as the Reynolds number increases.

The line of particles near the IC has a higher degree of folding and stretching than those near the OC, most readily evident for  $\varepsilon = 1.48$  in Fig. 3(b). This probably results from the increased azimuthal velocity near the IC where the azimuthal velocity is substantially higher than the azimuthal wave speed, which is 0.3–0.4 times the speed of the IC [5,28,29]. Thus, in the period for one azimuthal wave,  $T$ , particles near the IC have traveled azimuthally farther than a single wave being exposed to more vortical transport and axial transport between vortices than particles initially near the OC. This result is amplified considering the azimuthal transport of the line of particles in Fig. 4, which shows the position of the axial line of particles collapsed into a single latitudinal plane. The axial line of particles initially appears as a single point near the right side of the circular section. After just  $0.5T$  the line of particles has stretched azimuthally and extends across nearly the entire annular gap regardless of the initial radial position. However, particles initially near the IC have traveled farther azimuthally. By  $1.0T$  the particles initially near the IC have stretched more than those starting near the OC. Of course, the chaotic mixing carries particles initially near the IC to the OC and vice versa, so in the long run the effect of the initial radial position is lost.

The positions of the same three axial lines of particles on an unwrapped circumferential surface are shown in Fig. 5. For reference, the azimuthal wavelength corresponding to an azimuthal wave is  $\lambda_\theta = [r_i + (d/2)]2\pi/m = 7.94d$  for  $m = 4$  waves. Since

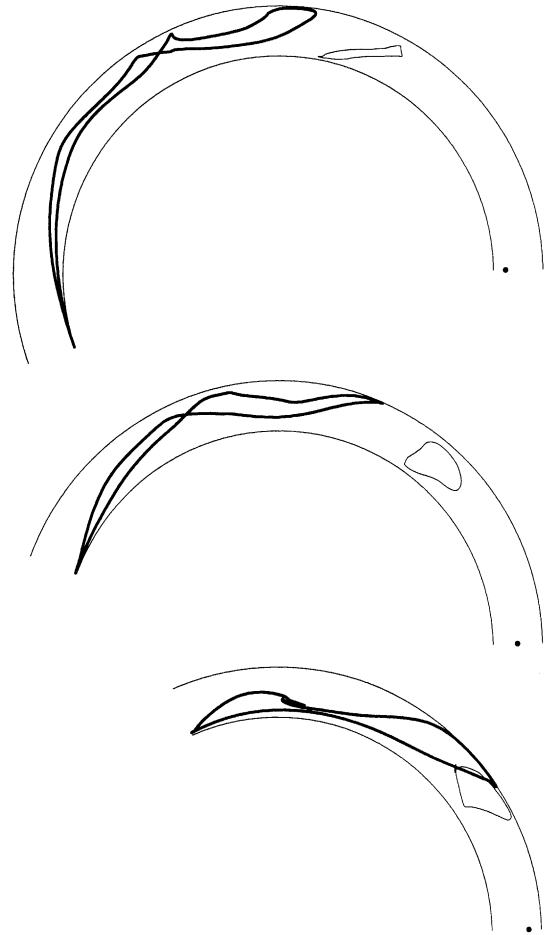


Fig. 4. Deformation of an axial line of 2000 particles initially about  $2\lambda$  long at  $(r - r_i)/d = 0.25$  (top),  $0.5$  (middle),  $0.75$  (bottom) for  $t = 0$  (single dot),  $0.5T$  (fine curve), and  $1.0T$  (bold curve) viewed in a latitudinal plane for  $\varepsilon = 1.48$ .

the original line extends two axial wavelengths (four vortices), the shape of the stretched line of particles is periodic in the axial direction with period  $2d$ . Some of the particles starting at  $(r - r_i)/d = 0.25$  have traveled nearly one full azimuthal wavelength due to the higher azimuthal velocity by  $0.5T$ , whereas particles starting near  $(r - r_i)/d = 0.75$  have traveled only half as far. By  $1.0T$  the axial line of particles has stretched azimuthally by about one full azimuthal wavelength, with the greatest stretching for the line of particles initially near the IC. Clearly the stretching is not uniform, based on the distance between dots at  $1.0T$ . The

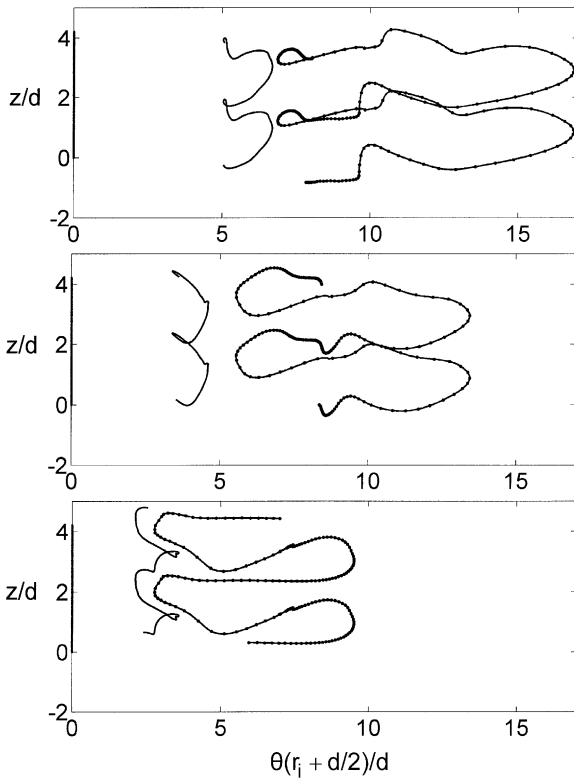


Fig. 5. Deformation of an axial line of 2000 particles initially  $2\lambda$  long at  $(r - r_i)/d = 0.25$  (top),  $0.5$  (middle),  $0.75$  (bottom) for  $t = 0$  (vertical line at  $\theta = 0$ ),  $0.5T$  (middle curve), and  $1.0T$  (right curve) viewed in an unwrapped circumferential surface at the center of the annular gap for  $\varepsilon = 1.48$ . Dots on the lines denote every 10th particle.

portions of the curve that are stretched significantly are those close to the IC as viewed in Fig. 4. It is also evident that some particles have moved axially beyond the extent of the original line, but the axial stretching is small compared to the azimuthal stretching.

We can also consider the deformation of a line of 1000 particles initially positioned along a radius across the annular gap, shown in Fig. 6 for  $\varepsilon = 1.48$ . Like previous cases, we consider a line of fluid particles “released” at an initial azimuthal position corresponding to the meridional plane in which the azimuthal wave is at its rightmost axial position. In this case, the radial line of particles is released from the following initial axial positions with respect to a vortex pair: (i) the center (C) of a CW vortex; (ii) an inflow

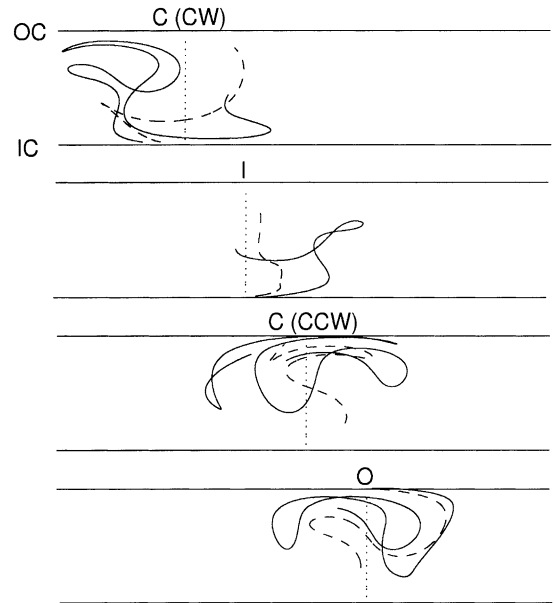


Fig. 6. Deformation of a radial line of 1000 particles initially positioned at a clockwise vortex center [C(CW)], an inflow boundary [I], a counter-clockwise vortex center [C(CCW)], and an outflow boundary [O] for  $t = 0$  (dotted),  $0.5T$  (dashed), and  $1.0T$  (solid) viewed in a meridional plane for  $\varepsilon = 1.48$ .

boundary (I); (iii) the center of a counter-clockwise (CCW) vortex; and (iv) an outflow boundary (O). Of course, since the vortices are wavy, these axial positions only align with these locations with respect to the vortex pair at the instant the particles are released. Significant stretching and folding is evident in Fig. 6 for both vortex centers and for the outflow boundary. However, the line of particles at the inflow boundary undergoes much less folding and stretching. This result occurs for all Reynolds numbers and independent of when the particles are released with respect to the phase of the azimuthal wave. This result is surprising given our earlier explanation that fluid near the IC is carried farther azimuthally in a given time exposing it to more waves to fold and stretch the line.

More insight is obtained from observing the stretching in a latitudinal plane, shown in Fig. 7. The length of the arc shown in the figure clearly indicates that the particles in the radial line at an inflow boundary are stretched further azimuthally than particles at a vortex center or outflow boundary. Yet there

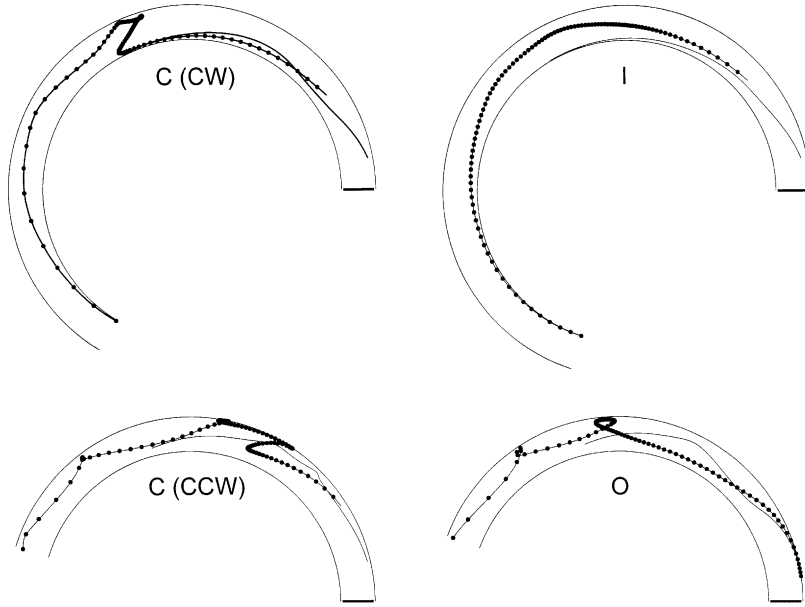


Fig. 7. Deformation of a radial line of 1000 particles initially positioned at a clockwise vortex center [C(CW)], an inflow boundary [I], a counter-clockwise vortex center [C(CCW)], and an outflow boundary [O] for  $t = 0$  (bold radial line),  $0.5T$  (curve with no dots), and  $1.0T$  (curve with dots denoting every 10th particle) viewed in a latitudinal plane for  $\varepsilon = 1.48$ .

is substantially less folding evident for the line of particles at an inflow boundary. The reason for little folding at an inflow boundary is not clear. Close inspection of the velocity field at inflow boundaries through several meridional slices of a wave does not reveal a substantially different appearance from outflow boundaries (other than the sense of the velocity) [6]. There are however two significant differences in the velocity field at inflow and outflow boundaries. First, the outflow is generally stronger than the inflow [30]. Second, the redistribution of azimuthal momentum by the vortical motion results in either a velocity defect or a velocity augmentation compared to the stable, nonvortical velocity field. The velocity defect at an inflow boundary is greater than the velocity augmentation at an outflow boundary [6]. However, neither of these differences between inflow and outflow boundaries suitably explains the minimal folding at an inflow boundary. It appears that particles initially in a radial line at an inflow boundary are carried toward the IC and then stretched substantially by the high azimuthal velocity before vortical motion carries the particles outward again to provide any folding.

## 5. Stretching

It is possible to quantify the stretching by simply comparing the length of a line of fluid particles at some time  $t$  with the initial length of the same line of particles at  $t = 0$ . Thus, we calculate the stretch,  $S_n$ , at time increment  $n$  as

$$S(n) = \frac{\sum_j |X(n)|}{\sum_j |X(0)|}, \quad j = 2 : N, \quad (2)$$

where the distance between two adjacent particles  $j$  and  $j - 1$  at time increment  $n$  is

$$|X(n)| = \left[ (r_j(n) - r_{j-1}(n))^2 + (r_j(n)\theta_j(n) - r_{j-1}(n)\theta_{j-1}(n))^2 + (z_j(n) - z_{j-1}(n))^2 \right]^{1/2}. \quad (3)$$

The denominator of Eq. (1) is the initial length of the line at  $t = 0$ . The degree of stretching as a function of time is shown in Fig. 8 for the three different reduced Reynolds numbers considered. In this case, the time axis is nondimensionalized with the rotational

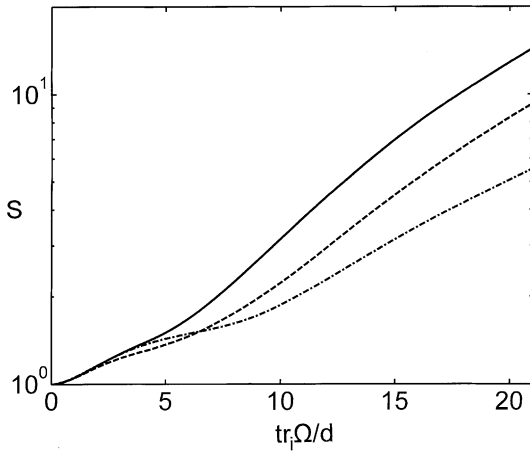


Fig. 8. Stretching as a function of time for  $\varepsilon = 0.28$  (dashed-dot),  $\varepsilon = 1.48$  (dashed), and  $\varepsilon = 5.03$  (solid).

speed rather than the period for an azimuthal wave,  $T$ , to permit comparison between Reynolds numbers having different numbers of azimuthal waves. At each Reynolds number, the stretching was calculated for an axial line like that in Figs. 3–5 at three initial radial positions,  $(r - r_i)/d = 0.25, 0.50, 0.75$  and then averaged. First, it is evident that the stretching grows approximately exponentially with time after an initial period of slower growth in all cases, as would be expected for a chaotic system. (The slight downward curvature at longer times may be a consequence of particles getting computationally

“stuck” on the wall and, consequently, not having the distance between them change with time.) Second, the stretching increases with increasing Reynolds number.

## 6. Mixing

Insight into the enhanced axial transport in WVF can be obtained by tracking particles over time. Fig. 9 shows the positions of 1250 particles initially distributed along a single axial line  $\lambda$  long (two vortices) at the middle of the annulus over 2, 4, 6, and 8T at  $\varepsilon = 1.48$ . (Particles “sticking” to the walls is a nonphysical artifact that comes about when the particles get so close to the wall that there is essentially no radial velocity at the resolution of the computational grid that can carry them away from the wall.) In addition to the very quick inter-vortex mixing, it is evident that by 8T, particles have penetrated eight vortices via intra-vortex mixing.

The combination of the azimuthal velocity, the azimuthal waviness, and the transport between vortices results in enhanced axial dispersion of fluid particles and mixing. The axial transport can be quantified in terms of an “axial dispersion” coefficient, also known as an “effective diffusion” coefficient. The axial dispersion coefficient is based on the chaotic advection of a large number of fluid particles using the

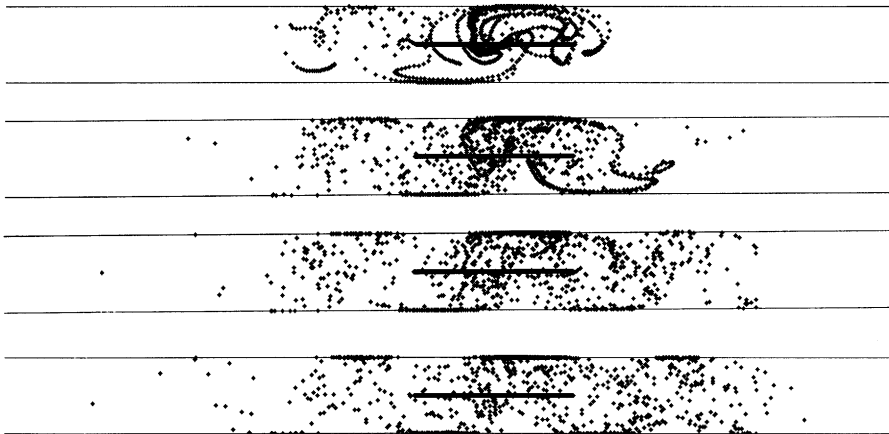


Fig. 9. Positions of 1250 particles initially on an axial line at  $(r - r_i)/d = 0.5$  after 2, 4, 6, and 8T for  $\varepsilon = 1.48$  viewed in a meridional plane.

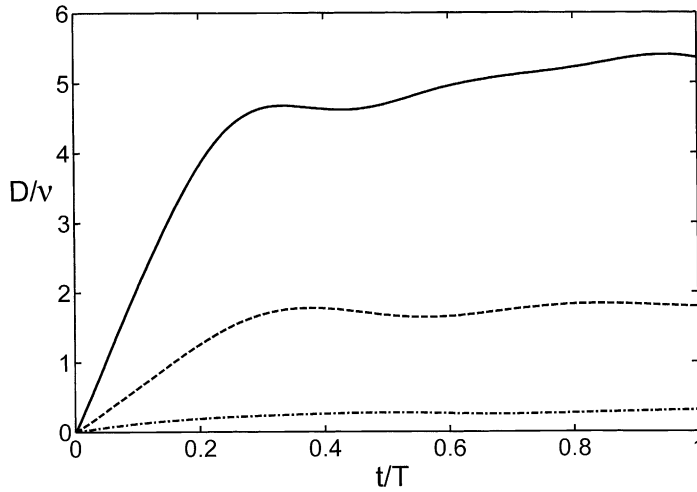


Fig. 10. Instantaneous axial dispersion as a function of time for  $\varepsilon = 0.28$  (dashed-dot),  $\varepsilon = 1.48$  (dashed), and  $\varepsilon = 5.03$  (solid).

expression [7]:

$$D' = \lim_{n \rightarrow \infty} \{D(n\Delta t)\} \\ = \lim_{n \rightarrow \infty} \left\{ \frac{1}{N} \sum \frac{[z_j(n) - z_j(0)]^2}{2n\Delta t} \right\}, \quad (4)$$

where  $N$  is the total number of particles and  $z_j(n)$  the dimensional axial position of the  $j$ th particle at time step  $n$ . The axial dispersion is shown in Fig. 10 as a function of time for the three Reynolds numbers that we considered. The instantaneous dispersion coefficient  $D$  necessarily starts very small for small  $t = n\Delta t$  as particles move only a short distance from their initial position. In addition, at small  $t$ , the axial dispersion coefficient depends on the initial positions of the particles. Thus, the results in Fig. 10 are the average of three axial lines of particles at the three radial positions in Fig. 3 to avoid errors due to the initial position of the particles.

After a short transient of  $t \approx 0.35T$ ,  $D$  reaches a value  $D'$  that is indicative of axial mixing due to chaotic transport of the particles, much like the molecular diffusion coefficient is indicative of mixing due to molecular diffusion. Because small experimental errors are likely to be magnified during numerical integration of the experimentally obtained velocity field, we calculate the argument of the limit in the

expression for the axial dispersion coefficient  $D(n\Delta t)$  as a function of time only up to  $t = 1.0T$ . The short transient is consistent with computational models of particle transport in wavy vortex flow [10] where the axial dispersion coefficient became essentially independent of time for  $tr_i\Omega/d > 10$  (corresponding to about  $0.5T$  or less), although our previous calculations based on a phenomenological model of wavy vortex flow required a longer time to reach their final value [11]. The nonphysical sticking of particles to the walls is insignificant at  $1.0T$  (only about 0.7% of the particles), so this does not affect the dispersion coefficient.

The values at  $1.0T$  in Fig. 10 are quite similar to those obtained experimentally and computationally for axial dispersion. Using the residence time distribution of a tracer, Moore and Cooney [1] found axial dispersion coefficients for  $\eta = 0.81$  ranging from  $0.05 \text{ cm}^2/\text{s}$  at  $\varepsilon = 2.24$  to  $0.11 \text{ cm}^2/\text{s}$  at  $\varepsilon = 6.38$ , consistent with our values of  $0.06 \text{ cm}^2/\text{s}$  at  $\varepsilon = 1.48$  and  $0.17 \text{ cm}^2/\text{s}$  at  $\varepsilon = 5.03$  for  $\nu = 0.031 \text{ cm}^2/\text{s}$ . For comparison, the molecular diffusion coefficient for glycerol in water is  $\sim 10^{-3} \text{ cm}^2/\text{s}$  indicating that transport due to chaotic advection is significantly greater than transport due to molecular diffusion.

Perhaps a better comparison is in terms of the Schmidt number based on the effective axial dispersion,  $Sc = \nu/D'$ , as shown in Fig. 11 for experimental

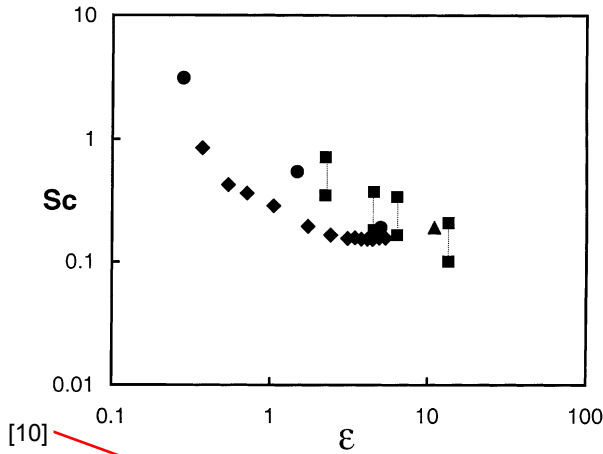


Fig. 11. Schmidt number as a function of the reduced Reynolds number.  $\blacklozenge$ , computational [10];  $\blacksquare$ , dye diffusion [1] (vertical distribution represents the range of possible values since the exact viscosity was not provided by the authors);  $\blacktriangle$ , dye diffusion [22];  $\bullet$ , current results.

[1,22] and computational results [10]. Using a computational model of wavy vortex flow, Rudman found that  $Sc$  decreased from 0.85 at  $\varepsilon = 0.37$  to a constant value of 0.15 for  $3.10 \leq \varepsilon \leq 5.39$ , indicating the increasingly important role of chaotic transport with increasing Reynolds number [10]. Experimental results based on tracer diffusion [1,22] and our results based on our particle tracking indicate somewhat higher Schmidt numbers, as shown in Fig. 11. However, the agreement between the computational results, experimental tracer results, and our particle tracking results is quite good given the different techniques to measure the Schmidt number and the range of conditions that were considered. Several comments are in order here. First, the high value of the Schmidt number at low  $\varepsilon$  where the wavy vortical motion is weak is not surprising, given that the Schmidt number asymptotes to a very high value for no chaotic transport at all. For example, the molecular diffusion coefficient for glycerol in pure water is quite small leading to  $Sc \sim 10^3$ . Secondly, Moore and Cooney [1] only provided a range of viscosities for their experiments, so we plot a range of Schmidt numbers for their data. Finally, we would have liked to compare the results here to the results for the effective diffusion coefficient derived from our previous phenomenological model [11], but

those results are an order of magnitude smaller than the results of this and other studies indicating that the phenomenological model does not accurately describe the physics of axial dispersion. Measurements of the dispersion coefficient have also been made at much higher rotating Reynolds numbers ( $\varepsilon > 10$ ) in the turbulent Taylor vortex flow regime. The axial dispersion coefficient for these cases is much greater than that for wavy cylindrical Couette flow [1,17,18,21,22]. The mechanism for enhanced transport in turbulent Taylor vortex flow is doubtless intrinsic to the turbulence, whereas the mechanism in wavy vortex flow is axial transport of fluid between wavy vortices.

## 7. Summary

As experimental techniques that are applied to classic fluid dynamics problems become increasingly sophisticated, so too should analytic techniques adapt and develop. Our approach is intended to provide a picture of the nature of the mixing and axial transport properties of wavy cylindrical Couette flow. The unique aspect of this work is that we have tracked particles in an experimentally measured time-resolved velocity field in three dimensions rather than a computational, theoretical, or phenomenological model of the flow. Thus, the degree of vortex distortion and transport between vortices is based on physical measurements rather than perturbations of non-wavy vortices or computational models. Furthermore, our use of an experimental velocity field permits the consideration of flow conditions well above the transition from non-wavy Taylor–Couette flow to wavy vortex flow and for wider annular gaps, which is difficult using perturbation models.

Our results clearly show the chaotic nature of the flow. Material lines in the flow field stretch and fold resulting in horse-shoe structures. We show how the underlying circular Couette flow field affects the stretching and folding. A material line starting very near the IC is subject to more extensive folding than a material line initially near the OC because the higher azimuthal velocity near the IC carries the particles through more azimuthal waves. Of course, this effect is

smear out with time as the material line is dispersed radially. The degree of stretching and folding is dependent upon the Reynolds number. The vortex strength increases with Reynolds number, but this cannot be exclusively responsible for the chaotic advection. The enhanced axial dispersion requires that there be fluid transport between vortices. Since the axial transport of fluid between vortices reaches a maximum and then decreases somewhat with increasing Reynolds number [5,13], we can conclude that increasing vortex strength with Reynolds number combined with inter-vortex transport enhances chaotic advection as the Reynolds number increases. An interesting result is that a radial material line positioned at an inflow boundary is not exposed to as much folding as radial lines at vortex centers or an outflow boundary. It appears that this fluid is carried toward the IC and then swept with the IC rotation with little exposure to axial transport or vortical motion. Of course, this effect diminishes as the particles are redistributed in the vortex.

The effective dispersion coefficient calculated based on the axial dispersion of fluid particles provides results that are consistent with experimental measurements of the dispersion due to chaotic advection. The rate of axial scalar transport is increased substantially compared to that due to molecular diffusion. The enhancement of transport is largely due to the transfer of well-mixed fluid between adjacent wavy vortices. These results also indicate that the expression used to calculate the dispersion (Eq. (4)) provides a reasonable estimate of the experimentally determined dispersion due to chaotic advection.

## Acknowledgements

This work was supported by the National Science Foundation.

## References

- [1] C.M.V. Moore, C.L. Cooney, Axial dispersion in Taylor–Couette flow, *AIChE J.* 41 (1995) 723–727.
- [2] R.J. Campero, R.D. Vigil, Axial dispersion during low Reynolds number Taylor–Couette flow: intra-vortex mixing effects, *Chem. Eng. Sci.* 52 (1997) 3303–3310.
- [3] S. Lee, R.M. Lueptow, Rotating reverse osmosis: a dynamic model for flux and rejection, *J. Memb. Sci.* 192 (2001) 129–143.
- [4] P.S. Marcus, Simulation of Taylor–Couette flow. Part 2. Numerical results for wavy-vortex flow with one travelling wave, *J. Fluid Mech.* 146 (1984) 65–113.
- [5] S.T. Wereley, R.M. Lueptow, Spatio-temporal character of supercritical circular Couette flow, *J. Fluid Mech.* 364 (1998) 59–80.
- [6] A. Akonur, R.M. Lueptow, Three-dimensional velocity field for wavy Taylor–Couette flow, *J. Fluid Mech.*, submitted for publication.
- [7] D.S. Broomhead, S.C. Ryrie, Particle paths in wavy vortices, *Nonlinearity* 1 (1988) 409–434.
- [8] S.C. Ryrie, Mixing by chaotic advection in a class of spatially periodic flows, *J. Fluid Mech.* 236 (1992) 1–26.
- [9] P. Ashwin, G.P. King, A study of particle paths in non-axisymmetric Taylor–Couette flows, *J. Fluid Mech.* 338 (1997) 341–362.
- [10] M. Rudman, Mixing and particle dispersion in the wavy vortex regime of Taylor–Couette flow, *AIChE J.* 44 (1998) 1015–1026.
- [11] M. Rudolph, T. Shinbrot, R.M. Lueptow, A model of mixing and transport in wavy Taylor–Couette flow, *Physica D* 121 (1998) 163–174.
- [12] G.P. King, G. Rowlands, M. Rudman, A.N. Yannacopoulos, Predicting chaotic dispersion with Eulerian symmetry measures: wavy Taylor–vortex flow, *Phys. Fluids* 13 (2001) 2522–2528.
- [13] I. Mezic, Chaotic advection in bounded Navier–Stokes flows, *J. Fluid Mech.* 431 (2001) 347–370.
- [14] T.H. Solomon, J.P. Gollub, Passive transport in steady Rayleigh–Bénard convection, *Phys. Fluids* 31 (1988) 1372–1379.
- [15] T.H. Solomon, J.P. Gollub, Chaotic particle transport in time-dependent Rayleigh–Bénard convection, *Phys. Rev. A* 38 (1988) 6280–6286.
- [16] A. Davey, R.C. DiPrima, J.T. Stuart, On the instability of Taylor vortices, *J. Fluid Mech.* 31 (1968) 17–52.
- [17] W.Y. Tam, H.L. Swinney, Mass transport in turbulent Couette–Taylor flow, *Phys. Rev. A* 36 (1987) 1374–1381.
- [18] Y. Enokida, K. Nakata, A. Suzuki, Axial turbulent diffusion in fluid between rotating coaxial cylinders, *AIChE J.* 35 (1989) 1211–1214.
- [19] R.D. Vigil, Q. Ouyang, H.L. Swinney, Spatial variation of a short-lived intermediate chemical species in a Couette reactor, *J. Chem. Phys.* 96 (1992) 6126–6131.
- [20] R.M. Lueptow, A. Hajiloo, Flow in a rotating membrane plasma separator, *Am. Soc. Artif. Int. Organs J.* 41 (1995) 182–188.
- [21] G. Desmet, H. Verelst, G.V. Baron, Local and global dispersion effects in Couette–Taylor flow. II. Quantitative measurements and discussion of the reactor performance, *Chem. Eng. Sci.* 51 (1996) 1299–1309.
- [22] N. Ohmura, K. Kataoka, Y. Shibata, T. Makino, Effective mass diffusion over cell boundaries in a Taylor–Couette flow system, *Chem. Eng. Sci.* 52 (1997) 1757–1765.
- [23] R.C. Giordano, R.L.C. Giordano, D.M.F. Prazeres, C.L. Cooney, Analysis of a Taylor–Poiseuille vortex flow reactor.

- I. Flow patterns and mass transfer characteristics, *Chem. Eng. Sci.* 53 (1998) 3635–3652.
- [24] A. Recktenwald, M. Lücke, H.W. Müller, Taylor vortex formation in axial through-flow: linear and weakly nonlinear analysis, *Phys. Rev. E* 48 (1993) 4444–4454.
- [25] A. Souvaliotis, S.C. Jana, J.M. Ottino, Potentialities and limitations of mixing simulations, *AIChE J.* 41 (1995) 1605–1621.
- [26] S. Smale, Differentiable dynamical systems, *Bull. Am. Math. Soc.* 73 (1967) 747–817.
- [27] J.M. Ottino, *The Kinematics of Mixing: Stretching, Chaos, and Transport*, Cambridge University Press, Cambridge, 1989.
- [28] D. Coles, Transition in circular Couette flow, *J. Fluid Mech.* 21 (1965) 385–425.
- [29] G.P. King, Y. Li, W. Lee, H.L. Swinney, P.S. Marcus, Wave speeds in wavy Taylor-vortex flow, *J. Fluid Mech.* 141 (1984) 365–390.
- [30] S.T. Wereley, R.M. Lueptow, Azimuthal velocity in supercritical circular Couette flow, *Exp. Fluids* 18 (1994) 1–9.